Stability threshold for stratification-induced flowrate oscillations in PLANDTL-2 sodium natural circulation experiment

S Renaudière de Vaux, Simon Li, Amandine Marrel, Toshiki Ezure, Masaaki Tanaka

To cite this version:

S Renaudière de Vaux, Simon Li, Amandine Marrel, Toshiki Ezure, Masaaki Tanaka. Stability threshold for stratification-induced flowrate oscillations in PLANDTL-2 sodium natural circulation experiment. 2025. ⟨cea-05084224⟩

HAL Id: cea-05084224

https://cea.hal.science/cea-05084224v1

Preprint submitted on 26 May 2025

Stability threshold for stratification-induced flowrate oscillations in PLANDTL-2 sodium natural circulation experiment

S. Renaudière de Vaux[a,*], S. Li[a], A. Marrel[a], T. Ezure[b], M. Tanaka[b]

[a] *CEA, DES, IRESNE, DER, Cadarache, France*
[b] *Japan Atomic Energy Agency (JAEA) of Oarai, Japan*

Abstract

Thermal stratification in the hot and cold pools of sodium-cooled reactors during loss of flow accidental transients competes with natural circulation and might affect the reactor core cooling. One of the goals of the PLANDTL-2 facility is to study this type of issues, in an integral configuration, representative of a reactor case. In this paper, experimental results on sodium natural circulation in PLANDTL-2 are reported. Eight transient scenarios are studied. The investigated parameters are the initial state of the primary circuit, the shutdown inertia of the secondary circuit, and the operating mode of the Decay Heat Removal (DHR) system. It appears that in cases where the heat removal via the DHR circuit is the highest, flow reversals can be observed in the primary circuit, in the long-term range, more than 100 min after the transient starts. These thermalhydraulic instabilities are linked to an enhancement of stratification caused by the strong heat removal at the DHR system, leading to a cliff effect, both on thermal stratification and primary flowrate. Counter-intuitively, to avoid the apparition of these instabilities, the heat removal via the DHR system should be delayed, after the full establishment of natural circulation. A novel method is introduced to estimate the delay between DHR system activation and increase in stratification. The results show that smaller power ramps favor flow stability. Finally, some guidelines for future investigations are given in order to avoid the presently described instabilities. Prospective tests are also proposed to study more in depth this cliff effect.

Keywords: Natural circulation, sodium loop, thermal-hydraulics, stability, experiment

---

[*] Corresponding author
Email address: `sebastien.renaudieredevaux@cea.fr` (S. Renaudière de Vaux)

Nomenclature

Abbreviations and acronyms

AC	Air Cooler (ultimate heat sink)
CEA	Commissariat à l'Énergie Atomique et aux Énergies Alternatives
CFD	Computational Fluid Dynamics
DHR	Decay Heat Removal
DHX	Dipped Heat eXchanger
EMF	ElectroMagnetic Flowmeter
EMP	ElectroMagnetic Pump
HEX	Heat EXchanger
IET	Integral Effect Test
IHX	Intermediate Heat eXchanger
IWG	InterWrapper Gap
JAEA	Japan Atomic Energy Agency
PLANDTL-2	Plant Dynamics Test Loop 2
UIS	Upper Internal Structure

Greek letters

β	Thermal expansion coefficient, [K^{-1}]
κ	Thermal diffusivity, [m^2/s]
λ	Thermal conductivity, [W/m.K]
μ	Dynamic viscosity, [Pa.s]
ν	Kinematic viscosity, [m^2/s]
ρ	Density, [kg/m^3]
τ	System response time, [s]

Latin letters

$\dot{Q}$	Power, [W]
A, B	Normalized signals, [-]
c_p	Heat capacity, [J/K]
H	Height, [m]
h	Heat transfer coefficient, [W/m^2.K]
T	Temperature, [°C]
U	Velocity, [m/s]
W	Mass flowrate, [kg/s]

Nondimensional numbers

Gr	Grashof number, $D_I^2\rho^2\beta g\Delta T/\mu^2$
Nu	Nusselt number, hH/λ
Pr	Prandtl number, ν/κ
Ra	Rayleigh number
Re	Reynolds number
St	Stanton number, $\mathrm{Nu}/(\mathrm{Re}\,\mathrm{Pr})$

Subscripts

core	relative to the core
DHX, *IHX*	relative to the DHX, the IHX
heat, *unheat*	relative to the heated and unheated channels
I, *II*	relative to primary, secondary circuit
in	inlet
out	outlet
pl	plenum
r	reference

1. Introduction

Heat removal from the core during loss of flow accidental transients in nuclear reactors is a crucial safety matter. Indeed, it is necessary to ensure that the core is properly cooled in order to avoid severe accident sequences, where the core, the assemblies and the structures supporting them can be irreversibly damaged. In this context, passive systems are promising as they avoid human intervention and the need for external energy sources to cool the reactor (i.e. electrical pumps). These systems operate in natural circulation and were adopted by several Sodium-cooled Fast Reactors (SFRs) concepts, including the ASTRID prototype [1, 2]. One way to passively remove the decay heat during an accidental transient is to use a Dipped Heat eXchanger (DHX) installed directly in the hot pool, as part of the Decay Heat Removal (DHR) system [3, 4].

In the context of liquid metal reactors, many challenges remain regarding the development and the design of such systems. For example, in order to properly model the 3D effects in the hot and cold pools of SFRs, Computational Fluid Dynamics (CFD) codes still require databases for validation [5]. Stratification in the pools is also the subject of active research for SFRs [6, 7], as well as for lead-cooled reactors [8, 9]. Indeed, thermal stratification in pool-type reactors may alter the primary flowrate [10–12]. In particular, in the case of primary pumps trips, natural circulation occurs and results show in addition that the Upper Internal Structure (UIS) plays a role in the mitigation of stratification [6]. The transition from forced to natural circulation is usually not well captured by system-scale codes and CFD (or multiscale simulations) is required [10]. In addition, large thermal fluctuations can be observed in the pool [13]. In worst cases, thermal stratification could impede the establishment of natural circulation, thus affecting the cooling of the core during accidental transients. Other experimental facilities such as STELLA-2 [14, 15] have highlighted possible strong stratification in the sodium pool. Similar conclusions were drawn thanks to CFD simulations of the lead-cooled facility CLEAR-S [8]. The typical approach to investigate numerically stratification was to use CFD of the pool [10, 16], or with multiscale simulations [2, 9]. Some more recent approaches dealt with the 1D modeling of stratification [10–12]. This type of approach could enable more computationally accessible methods, compared to CFD or multiscale simulations.

Experimentally, it has been shown on the previous configuration of the PLANDTL (Plant Dynamics Test Loop) facility (studied here), that the interwrapper gap flow (IWG flow) could significantly contribute to the core cooling, due to lateral fluid motion [17]. In a more recent configuration of the facility, called PLANDTL-2, the effect of the DHR system was monitored [18]. The results highlighted that the radial distribution of the temperature at the exit of the core was relatively flat, confirming that the IWG flow contributes significantly to the core cooling, in the presence of the DHX. The stability of passive systems, which is necessary in order to ensure the correct evacuation of decay heat to an ultimate heat sink, is of particular interest. Instabilities in such systems can be of multiple types, usually related to two-phase instabilities [19, 20]. Such effects can be captured by system-scale codes [21, 22]. Instabilities also exist in 1D single-phase natural circulation [23–26]. Usual investigations of accidental transients focus on short ($t_{max} \approx 16$ min [8]) or medium-term phases ($t_{max} \approx 160$ min [9, 14]), but the long term behavior, $t_{max} \approx 600$ min, is often overlooked (except for example in [12]). In this paper, we report on the onset of instability and flow reversals due to strong thermal stratification in the hot pool of the PLANDTL-2 facility, with DHR systems operation. We identify cliff effects occurring on the long term, approximately 100 – 200 min after the start of the transient. In addition, the intuitive way to deal with an accidental scenario is to cool the hot pool quickly in order to remove the decay heat as fast as possible. We show here that this approach might lead to unstable behaviors and that, counter-intuitively, the cooling rate of the safety system should be moderated in the first hundreds of minutes of a transient in order to prevent flow instabilities.

In natural circulation cases, physical mechanisms at play need to be studied in depth to understand the system behavior, regarding heat transfer and flow paths. To address this matter, a sodium loop called PLANDTL-2 [27, 28], was developed by JAEA. This Integral Effect Test (IET) was designed to study the decay heat removal when the safety exchanger (thus the DHX) is dipped into the hot plenum; and also how the IWG flow could participate to the reactor cooling. In the framework of an international collaboration with CEA, the loop was used to study decay heat removal under several natural circulation conditions. The purpose is first to understand the dominant effects that govern natural circulation in PLANDTL-2, and second, to provide a validation database for multiscale computations. In this second context, preliminary analysis of experimental results is helpful to set up a modeling strategy, namely the use of system-scale codes, CFD codes or multiscale approaches [10–12]. Some conclusions are given in this paper to address these aspects.

Such loops are prone to instability [24, 26, 29], even in single-phase cases, as observed experimentally here (see Section 3.1). The stability boundaries are typically characterized by the Grashof Gr and Stanton St numbers. These nondimensional numbers compare different effects:

$$\mathrm{Gr} = \frac{\text{buoyancy effects}}{\text{viscous forces}}, \tag{1}$$

$$\mathrm{St} = \frac{\text{convective heat transfer}}{\text{heat capacity of the fluid}}. \tag{2}$$

The definition of each number is strongly case-dependent. In the case of PLANDTL-2, the effects of the IHX and the DHX have to be compared. The precise definitions of Gr and St will be discussed in Section 3.2.

As discussed later, the cases where instability and flow reversals were observed correspond to high St situations, contrary to the usual stability maps [24, 26, 29]. This counter-intuitive result originates primarily from the loop geometry. A physical mechanism involving the effect of thermal stratification is proposed and the experimental threshold is determined. Guidelines for future designs of sodium natural circulation loops and decay heat removal management are also given. In particular, in all cases, turning on the AC of the DHR system leads to an increase of the power extracted by the DHX, which increases the stratification. The response time of the system is not instantaneous, but depend on the jump in extracted power. To estimate the delay of the system response, we propose a new method inspired by a statistical dependence measure to extend the notion of deterministic cross-correlation usually used in signal processing to assess the similarities between two signals. Where standard correlation measures the simple linear similarity between signals as a function of a certain delay (between the two signals), the new proposed measure captures a broader spectrum of similarity. As a result, we find that the typical response time is of the order of magnitude of the typical timescales of buoyant structures. Furthermore, the higher the jump in power, the shorter the response time.

The loop geometry and test-cases are described in Section 2. Experimental results are presented in Section 3.1 and discussed in Sections 3.2 and 3.3. Final conclusions and guidelines are given in Section 4.

2. Loop and test-cases description

The loop is first presented in this section. Then, the transient test-cases are introduced.

2.1. Geometry and design of the loop

A simplified sketch of the PLANDTL-2 experimental setup is shown in Fig. 1. The test section is representative of pool-type SFRs, and the heat from nuclear fission is replaced by a simulated electrical core. Moreover, the primary loop is deported and the IHX is outside of the pool. The IHX is constituted of a tubes and shell Heat EXchanger (HEX) with baffle plates.

To simulate the pool behavior, four dummy cold legs are placed inside the hot pool to mimic the fluid-structure interaction. The DHX is dipped inside the hot pool and connected to the DHR circuit. Its role is to take over the IHX in accidental transients, in order to cool the hot pool and in term ensure removal of decay heat. As explained later, the DHR circuit and its AC can operate in several modes. In accidental situations the primary EMP is shut off and bypassed. The simulated core transfer a residual power of $\dot{Q}_{elec} = 110$ kW to the fluid.

In normal operation, the IHX ensures the cooling of the primary circuit, and the flow is forced by electromagnetic pumps (EMPs). During the accidental transients studied in this paper, the secondary side and the EMPs are shut down. The primary loop thus operates in natural circulation. In such cases, as presented later, there is a competition between the effects of the DHX on the cooling of the pool and thermal losses of

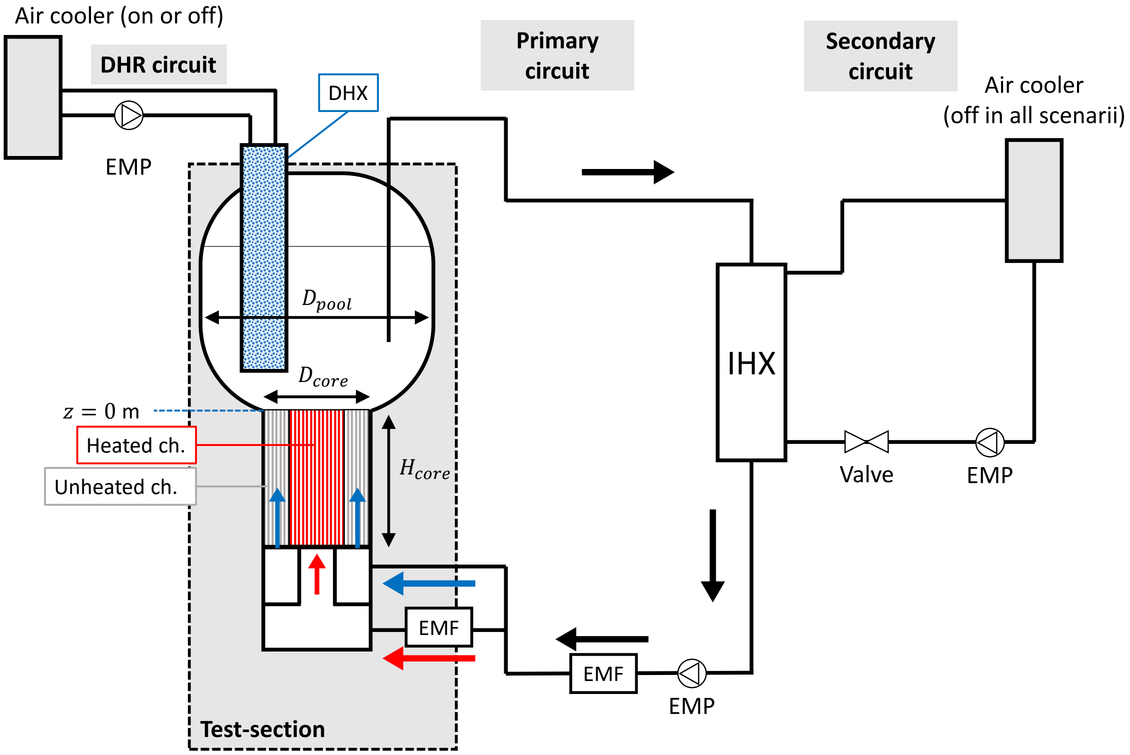

Figure 1: Simplified flow diagram in PLANDTL-2, as used in the present study. The upper internal structure (UIS) is not shown in the plenum for clarity. For convenience, only one HL is represented. Arrows indicate flow direction in nominal conditions. Not to scale. The EMPs and EMFs are indicated.

the IHX. As their elevation is higher than the core, they both provide a buoyancy driving term, entering in competition in ensuring circulation through the primary circuit and through the hot pool. A sketch of the hot pool is shown in Fig. 2. Two hot legs, at 180° from each other, collect the hot sodium in the pool towards the IHX. A close-up view on a vertical cross-section is shown in Fig. 2. The dimensions of the main components are summarized in Tab. 1. More details about the HEXs can be found in [18].

Table 1: Main dimensions of PLANDTL-2 loop.

Core diameter D_{core}	0.9 m
Core height H_{core}	0.9 m
Hot pool diameter D_{pool}	1.95 m
External DHX diameter D_{DHX}	0.27 m
HL inlet diameter	0.106 m

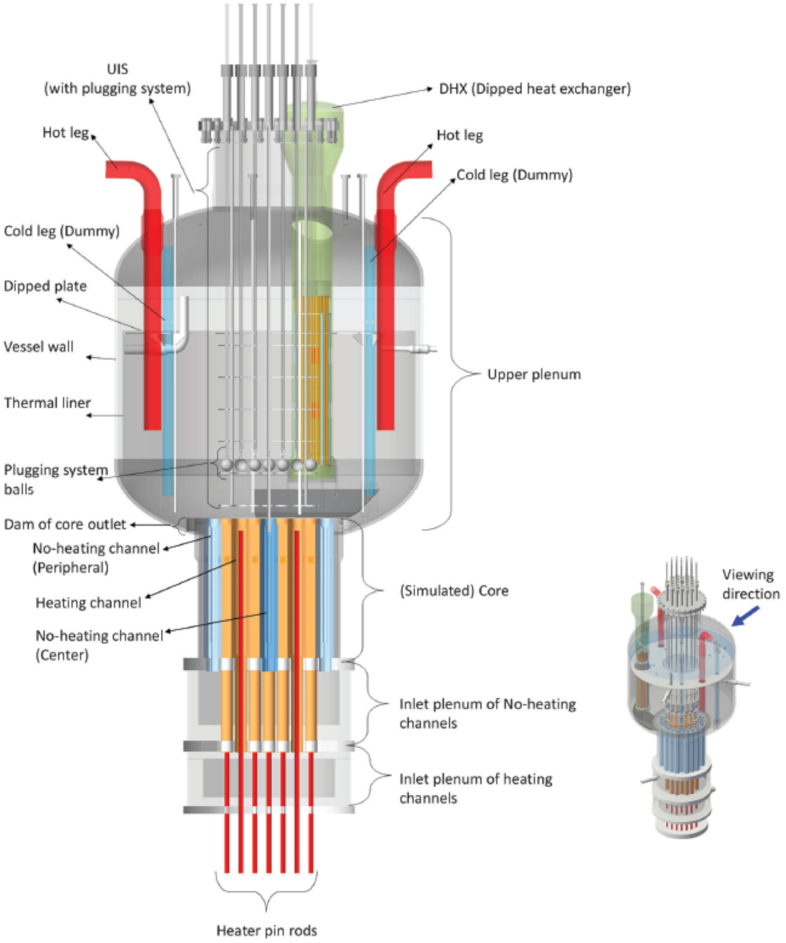

Figure 2: Cross-view of PLANDTL-2 test-section.

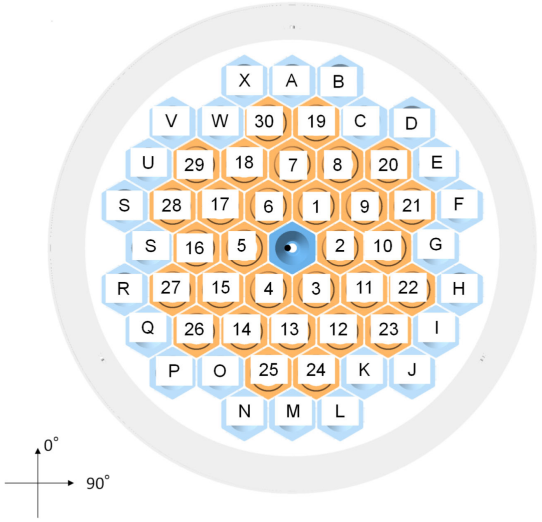

Figure 3: Heated (numbers) and unheated (letters + central) channels disposition in the simulated core.

The total primary flowrate W_I is measured upstream of the test-section, thanks to an electromagnetic flowmeter (EMF). Upstream of the core, the primary flow is divided in two, in order to feed separately the heated and unheated channels in the core, as shown in Fig. 1. The mass flowrate towards the unheated channels W_{heat} is measured by an EMF, and the flow through the heated channels W_{unheat} can be deduced by mass conservation, as:

$$W_I = W_{heat} + W_{unheat}. \tag{3}$$

The core is constituted of 30 electrically heated assemblies, placed on a hexagonal lattice. In addition, 24 non heated channels are placed at the outer core. The central rod is also not heated. A thermal liner is placed near the pool shell. A cross-sectional view of the simulated core is given in Fig. 3. Several ThermoCouples (TCs) and TC-trees are placed at key locations in the pipes, in the plenum and in the core. In particular, one TC-tree is placed near the HL inlet, as shown in Fig. 2.

Experimental data are recorded at a rate of 10 Hz during the first 3.5 hours of the transient. Then, after an interval of 15 min, data are further recorded at a sampling rate of 5 Hz for the next 7 hours, and so on. The 15 min interval is necessary due to data saving and the change of the record setting.

2.2. Transient test-cases

The typical transient scenario is as follows:

- Two initial primary flow conditions are tested, with an initial flowrate of 400 L/min or 800 L/min in the primary circuit;
- First, at the start of the transient, the primary pumps are stopped and bypassed;
- Then the secondary circuit valve is closed, and the AC of the secondary circuit is shut down. The time of secondary circuit closing is varied depending on the scenario. Two operating modes of the DHR circuit are investigated: in forced circulation along with the AC, or in natural circulation, with a delayed activation of the AC.

The transients can be described by three parameters, representing the aforementioned parameters. Eight accidental scenarios are investigated experimentally. The key features of each transient are summarized in Tab. 2. The three parameters of interest X_1-X_2-X_3 are respectively the initial temperature levels in the primary circuit X_1, the inertia of the secondary side X_2, and the operation of the DHR circuit in forced or natural circulation X_3. Each parameter X_i can take two values. To modulate each of these parameters X_i in practice, it was proceeded as follows:

- X_1: flowrate is imposed in the primary circuit prior to the startup of the test. It is either imposed at 800 L/min, or 400 L/min. As a result, the temperature levels in primary circuit are *cold* $X_1 = C$, or *hot* $X_1 = H$;
- X_2: the inertia of the secondary circuit is simulated by closing the regulating valve at $t = 100$ s, or at $t = 1000$ s. These two cases are referred as *low inertia cases* $X_2 = L$, or *inertial cases* $X_2 = I$;
- X_3: the operating mode of the air cooling in the DHR circuit is either in *forced circulation* $X_3 = F$, or in *natural circulation* $X_3 = N$.

The test conditions are summarized in Tab. 2.

Table 2: Experimental conditions.

Test ID	**Primary circuit**		**Secondary circuit**			**DHR circuit**	
	Flowrate (L/min)	Core power (kW)	Flowrate (L/min)	Valve closing time (s)	A/C power (kW)	Flowrate (L/min)	A/C power (kW)
C-I-F	$800 \xrightarrow{10\text{ s}} 0$	$500 \xrightarrow{10\text{ s}} 0$	$250 \xrightarrow{5\text{ s}} 0$	1000	$500 \xrightarrow{30\text{ s}} 0$	90	$0 \xrightarrow{620\text{ s}} 110$
C-L-F				100	$500 \xrightarrow{10\text{ s}} 0$		$0 \xrightarrow{620\text{ s}} 110$
H-I-F	$400 \xrightarrow{10\text{ s}} 0$			1000	$500 \xrightarrow{30\text{ s}} 0$		$0 \xrightarrow{620\text{ s}} 110$
H-L-F				100	$500 \xrightarrow{10\text{ s}} 0$		$0 \xrightarrow{620\text{ s}} 110$
C-I-N	$800 \xrightarrow{10\text{ s}} 0$			1000	$500 \xrightarrow{30\text{ s}} 0$	$90 \xrightarrow{10\text{ s}} 0$	$0 \xrightarrow{9600\text{ s}} 110$
C-L-N				100	$500 \xrightarrow{10\text{ s}} 0$		$0 \xrightarrow{620\text{ s}} 110$
H-I-N	$400 \xrightarrow{10\text{ s}} 0$			1000	$500 \xrightarrow{30\text{ s}} 0$		$0 \xrightarrow{9600\text{ s}} 110$
H-L-N				100	$500 \xrightarrow{10\text{ s}} 0$		$0 \xrightarrow{9600\text{ s}} 110$

3. Results and discussion

We discuss in this Section the experimental results and provide an interpretation for the observations. When used, values of thermo-physical properties (density, viscosity, etc.) of sodium are taken from [30].

3.1. Experimental results

The time-evolution of the flowrate in the primary circuit W_I is shown for all eight cases in Fig. 4, as well as W_{heat} and W_{unheat}. The initial value of the flowrate is $W_I = 5.7$ kg/s for hot cases (= 400 L/min) or $W_I = 11.4$ kg/s for cold cases (= 800 L/min). When the primary pump is stopped, the primary flowrate falls to $W_I \approx 0.05$ kg/s in a few minutes. For cases $X_3 = N$ where natural circulation occurs in the DHR circuit, after a quick decrease of W_I, the flowrate increases, until $t \approx 150 - 200$ min, then slowly decreases

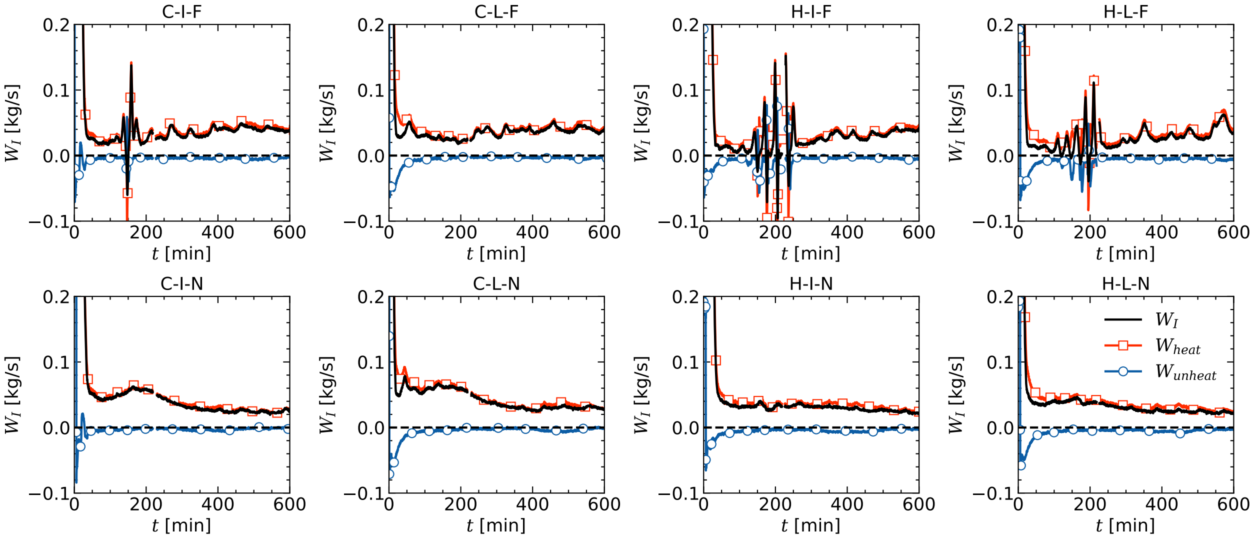

Figure 4: Primary flowrate.

over hundreds of minutes towards a steady-state value $W_I \approx 0.05$ kg/s. This local maximum is typical of natural circulation transients [2, 9]. The time-evolution is more complex in forced circulation cases $X_3 = F$. As a matter of fact, flowrate instability and reversals are observed from $t \approx 100$ min to $t \approx 220$ min, except for C-L-F. The reversals then stop and the flowrate remains quasi-steady, with irregular oscillations, with a typical oscillation timescale of ~ 20 min.

Moreover, it is seen that for all cases, $W_{heat} \approx W_I$. This means that most of the flowrate goes through the heated core channels, as it is driven by buoyancy (induced by the heating). Also, for all cases (except during the oscillation phase), $W_{unheat} < 0$ showing, that some fluid goes down through the outer channels. At it will be discussed, the counter-flow through the outer channels is caused by thermal stratification in the plenum. Indeed, colder and denser fluid accumulates near the bottom plenum wall, and dives near the external sides of the core.

Both the DHX and the IHX participate in the primary circuit cooling at different rate, but only the IHX provides a driving term for the natural circulation within the whole primary circuit. The DHX, due to its location, cools the plenum and generates a buoyancy term that lead to a secondary flow inside the hot pool, but not through the primary pipings. The temperature evolution at the inlet and outlet of the IHX, $T_{in,IHX}$ and $T_{out,IHX}$ respectively, is shown in Fig. 5. Here again, the temporal evolution depends on the natural or forced circulation in the DHX.

In $X_3 = N$ cases, $T_{out,IHX}$ decreases at the start, then reincreases and finally stabilizes around $T_{out,IHX} \approx 300$°C. For $T_{in,IHX}$, a slight decrease is observed, then an increase, and finaly a stabilization around $T_{in,IHX} \approx 400$°C. It is also observed that $\Delta T_{IHX} = T_{in,IHX} - T_{out,IHX}$ becomes small around $t \approx 100$ min, but there is

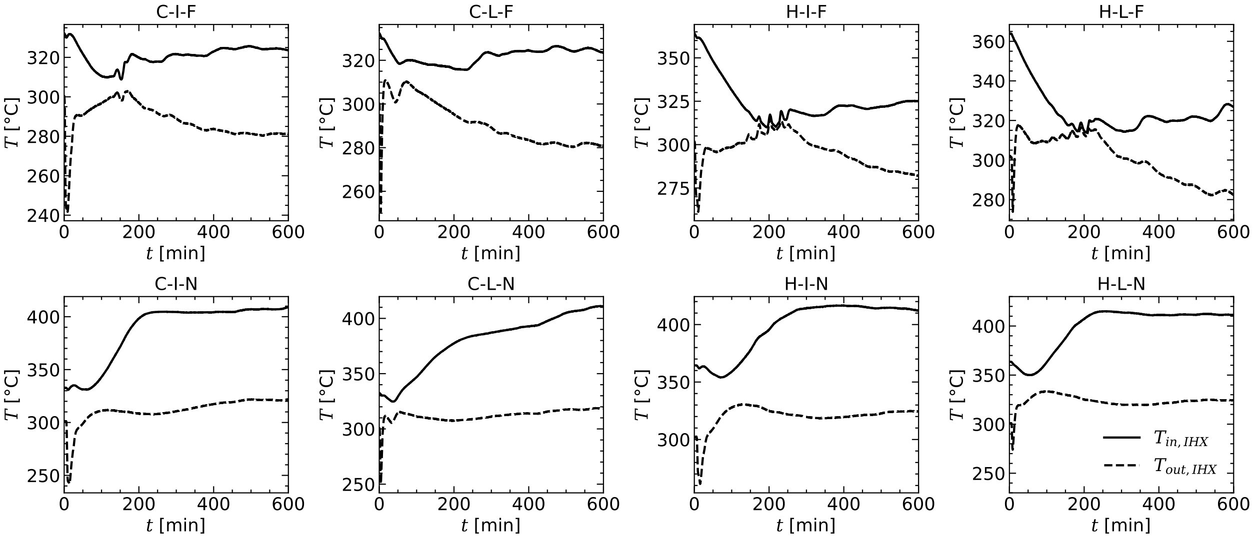

Figure 5: Temperature at inlet and outlet of the IHX (primary side).

no pinching and $\Delta T_{IHX} > 0$ for all cases.

This observation is not true for $X_3 = F$ cases. There, a steep decrease of $T_{in,IHX}$ is observed. Consequently, pinching is actually observed, $T_{in,IHX} \approx T_{out,IHX}$ between $t = 100$ min and $t = 220$ min approximately. The pinching is simultaneous with the flowrate oscillations from Fig. 4. Moreover it is observed that the pinching occurs earlier and the oscillations last longer in the $X_1 = H$ cases, than in the C cases. As a matter of fact, the cooling rate in H cases is higher, due to the larger temperature difference between the hot pool and the DHR circuit. As a consequence, $T_{in,IHX}$ decreases quicker than in $X_1 = C$ cases, and leads to the pinching.

The thermal power exchanged at the IHX is computed as:

$$\dot{Q}_{IHX} = W_I c_p \Delta T_{IHX}. \tag{4}$$

Its evolution over time is shown in Fig. 6. For all cases, it promptly decreases in less than 20 min, as the secondary circuit is closed. Because of the pinching in $X_3 = F$ cases, $\dot{Q}_{IHX}$ falls to zero during the pinching duration. It then increases to a quasi-steady value $\dot{Q}_{IHX} \approx 2$ kW. This is not the case for $X_3 = N$ cases. Indeed during the instability time frame 110 min $\leq t \leq$ 220 min, $\dot{Q}_{IHX}$ reincreases, reaches a maximum value and finally converges towards a similar quasi-steady value $\dot{Q}_{IHX} \approx 2$ kW.

Similarly, the power exchanged at the DHX is written as:

$$\dot{Q}_{DHX} = W_{DHX} c_p \Delta T_{DHX}, \tag{5}$$

with ΔT_{DHX} the temperature difference at the secondary side of the DHX. The DHX power evolution is shown in Fig. 7. First, the power removal by the DHX is an order of magnitude larger than the heat removed

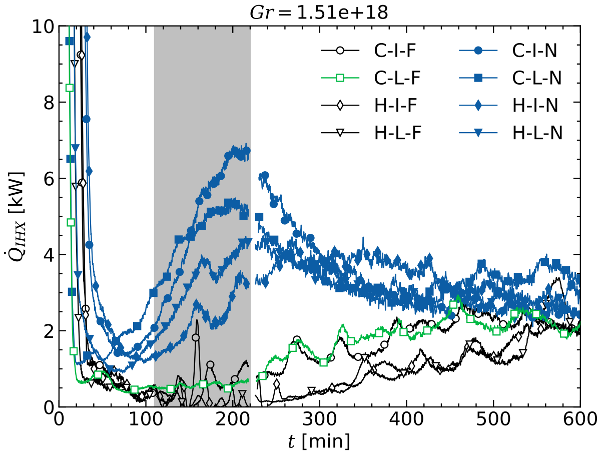

Figure 6: Exchanged power at the IHX over time. The instability time frame is indicated by the area shaded in grey.

by the IHX. Second, contrary to the IHX, it is not affected by the instability. This means that the heat transfer from the plenum to the DHX is not affected by the global circulation in the primary circuit. The power slowly increases for $X_3 = N$ cases. A steep jump is observed when the air-cooling is activated, at $t = 160$ min for *C-I-N*, *H-I-N* and *H-L-N*, and at $t = 10$ min 20 s for *C-L-N*. The jump is higher for $X_1 = H$ cases (around 60 kW), than for the *C-I-N* case (around 40 kW). Indeed, for $X_1 = H$ cases, the temperature difference between the primary circuit and the DHR circuit is higher than in the *C-I-N* case, leading to a higher increase in the heat flux $\dot{Q}_{DHX}$.

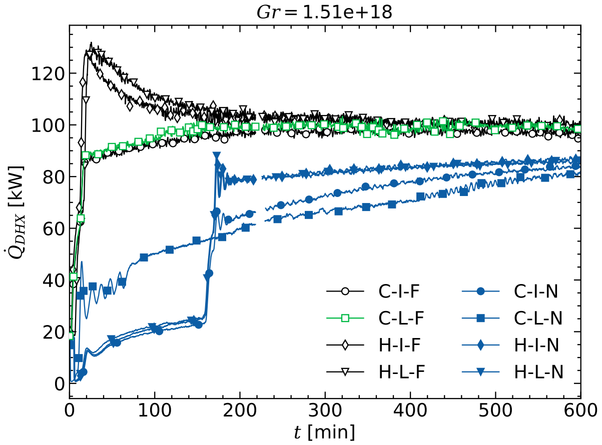

Figure 7: Exchanged power at the DHX over time.

For forced cases $X_3 = F$, the steep increases occur right after the start of the transient, as the flow is imposed in the DHR circuit. For forced hot cases *H-I-F* and *H-L-F*, the increase is steeper. Indeed, the temperature levels are higher in the primary circuit. Thus the temperature difference between the primary circuit and the DHR circuit is higher, as well as the heat flux. It is observed that, at the peak, $\dot{Q}_{DHX} \approx 125$ kW, which is larger than $\dot{Q}_{elec} = 110$ kW. This cold shock shows that on a global scale, the primary circuit is strongly cooled after the transient beginning.

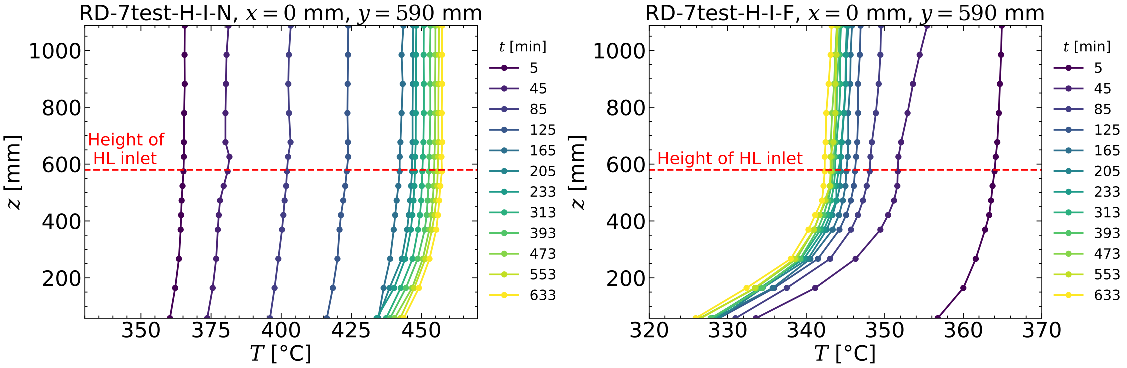

(a) *H-I-N*. (b) *H-I-F*.

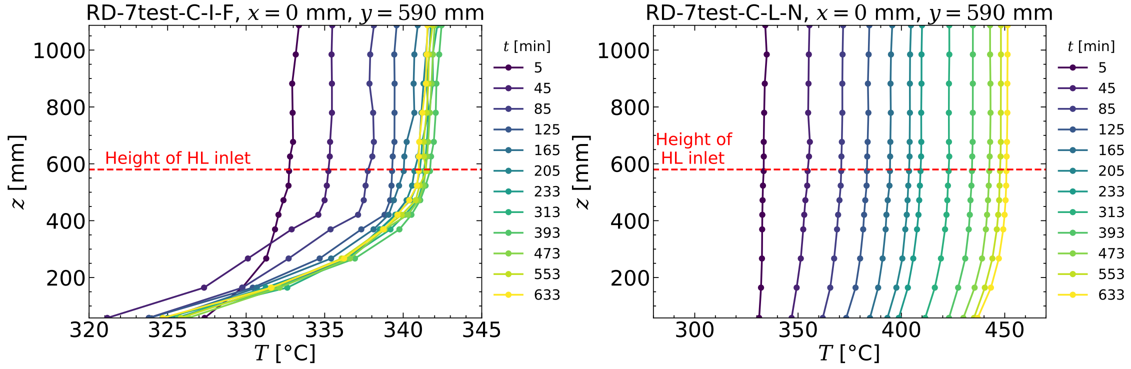

(c) *C-I-F*. (d) *C-L-N*.

Figure 8: Instantaneous vertical temperature profiles near the HL inlet.

In the following, we discuss specifically the cases *H-I-N*, *H-I-F*, *C-I-F* and *C-L-N*, which are representative of all cases. We show in Fig. 8 the instantaneous vertical temperature profiles near the HL inlet, as shown in Fig. 2, for the selected cases. This specific TC tree was chosen as it is near one of the HL inlet. However, comparison with the other TC trees in the plenum did not show significant differences in the azimuthal direction. The overall dynamics of the temperature strongly depends on the forced or natural circulation case, $X_3 = F$ or $X_3 = N$. In the case *H-I-N* the temperature levels rise from $T \approx 360$°C to ≈ 430°C at $t = 125$ min. Then, as the circulation in the DHR circuit is imposed, the rate of increase of the temperature levels in the plenum abruptly slows down and remains around $T \approx 450$°C.

For the $X_3 = N$ cases, the final temperature levels are similar, $T \approx 450$°C. However, the rate at which the temperature rises differs, as shown by the successive shifts in the temperature profiles. First, in the *H-I-N* case, the temperature levels rise at a constant rate, until $t = 160$ min, when the DHR circuit AC is activated. After the activation, the rate at which the temperature increases drastically drops, as the successive profiles are closer. This is in agreement with the steep increase of $\dot{Q}_{DHX}$ (shown in Fig. 7) at $t = 160$ min for *H-I-N*, as more thermal energy is removed. On the opposite, the rate of temperature increase in the *C-L-N* case is constant during the whole transient. Indeed, the DHR circuit AC is turned on at the beginning of the transient, after $t = 10$ min 20 s. The increase rate is coherent with the value of $\dot{Q}_{DHX}$ for this case, which is comprised between the value of $\dot{Q}_{DHX}$ for the case *H-I-N*, before and after the AC activation, as shown in Fig. 7.

In the *H-I-F* case, the DHR circulation is immediately imposed. As a consequence, the temperature levels in the plenum quickly drop from $T \approx 365$°C to ≈ 340°C. The dynamics in the *C-I-F* case is opposite to this. It is observed that the temperature levels increase quickly to reach the same temperature levels as in *H-I-F*. This difference is due to the difference in initial condition, $X_1 = C$ or H. Nevertheless, all *F* cases converge towards the same final state. Similar conclusion was drawn for the *N* cases.

As reversals are observed in *H-I-F* and *C-I-F*, it can be concluded that the overall temperature levels are not only responsible for the apparition of the reversals. As seen from the height of the HL inlet and the shape of the temperature profile with colder temperature near the bottom, this shows that stratification in the plenum plays a key role.

The evolution of the vertical temperature gradient near the HL is shown in Fig. 9 for the selected cases. It highlights the stratification level in the plenum. With the chosen coordinate system, with z in the upward direction, $dT/dz > 0$ indicates that the temperature increases with z. For each case, several profiles are shown, averaged over the indicated time window. The profiles are time-averraged over the selected temporal windows, as indicated in Fig. 9, in order to highlight the effect of the DHR circuit AC activation. At the start of the transient for the *H-I-N* case, the gradient is $dT/dz \approx 20$°C/m near the lower wall. It then decreases to values close to zero around $z \approx 600$ mm, and increases again slowly for higher z-values. When the transient starts, the stratification remains close to the initial stratification. When the DHX cooling is activated at $t = 160$ min, a quick shift in stratification is observed. The temperature gradient near the bottom is then $dT/dz \approx 50$°C/m, showing that colder fluid is at the bottom. Given the location of the HL inlet, colder fluid is therefore more likely to enter the HL. Moreover, it seen that the increased thermal stratification persists in time.

On the other hand, for the forced cases *H-I-F* and *C-I-F*, the forced circulation in the DHR circuit directly induces the shift in temperature gradient. Right after the start of the transient, the values of the gradient in the lower part are $dT/dz \approx 60$°C/m. It is noticeable that *H-I-F* and *C-I-F* have the same temporal evolution of the temperature gradients, and the same instantaneous gradients, despite having completely different temperature profiles. This highlights the enhancing effect of the DHR circuit on the stratification.

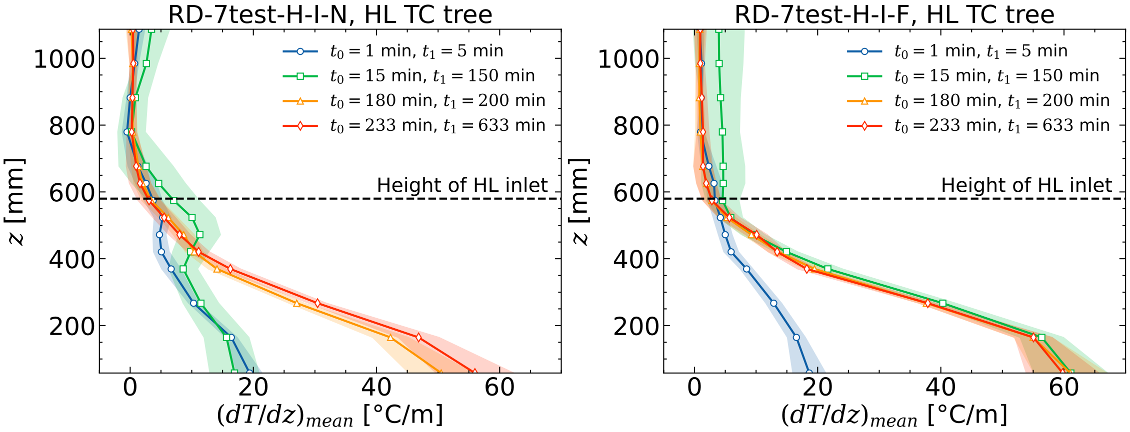

(a) *H-I-N*.

(b) *H-I-F*.

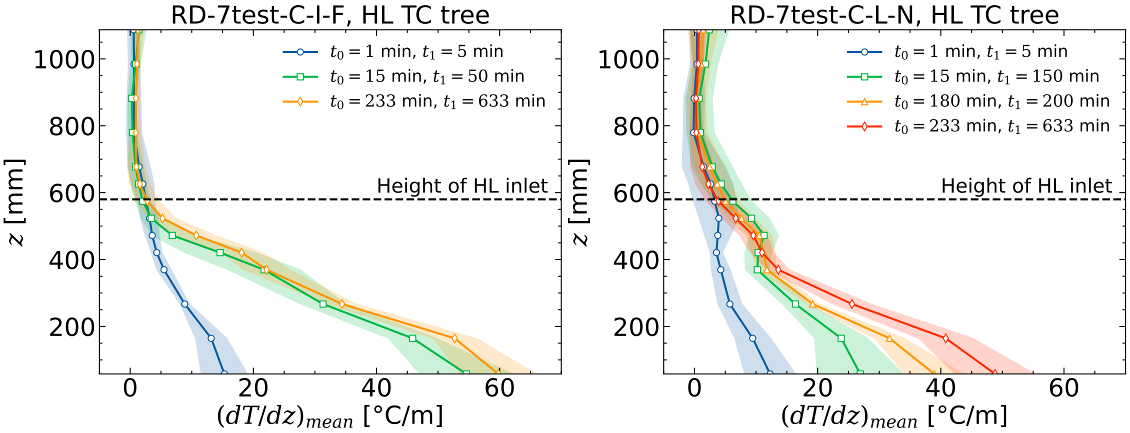

(c) *C-I-F*.

(d) *C-L-N*.

Figure 9: Vertical temperature gradient profiles near the HL inlet, time-averaged over the selected temporal windows. The shaded areas shows ± the Root-Mean Square value over the time frame.

In the *H-I-N* case, global natural circulation occurs when the fluid is rather homogeneous in temperature and is slowly cooled. On the other hand, for the case *H-I-F*, circulation occurs the fluid is highly stratified and is cooled quickly. The combination of these two effects leads to blocking the natural circulation through the IHX. This effect could be diminished if hotter fluid enters the HL, for example in a higher part of the plenum, or by mixing the fluid more efficiently in the plenum.

For the case *C-L-N*, one observes that the stratification increases progressively. In this case, the DHR circuit AC is activated earlier than in other $X_3 = N$ cases, at $t = 10$ min 20 s, against $t = 160$ min for the others. In this case, the DHR circuit is let free, and consequently the extracted power at the DHX has an intermediate value compared to N and F cases, as seen in Fig. 7. This confirms that the increase in $\dot{Q}_{DHX}$ enhances the thermal stratification.

In the end, the increase in $\dot{Q}_{DHX}$ can be achieved by activating the DHR circuit AC and/or imposing the circulation in it. The increase has thus two effects:

1. The overall heat transfer is increased, therefore the average temperature in the plenum quickly drops;
2. Due to its geometry, the DHX mainly cools the lower part of the plenum. Consequently, the plenum is highly stratified.

In all cases, it is observed that the stratification shift appears at the DHR activation, at $t = 10$ min for forced circulation cases, and at $t = 160$ min for natural circulation cases. The effect on the upper pool stratification is weak, and the latter remains similar to the situation before the activation of the DHR circuit AC.

In the *C-L-N* case, the increase in stratification is progressive, due to the early activation of the DHR circuit AC. An slower drift is observed, compared to other cases. Indeed, same stratification levels are reached, more than 200 min of transients, against in less than 10 min for the other cases.

In addition, it is seen that the temporal fluctuations remain weak, and that the thermal stratification is stable in time. Two key learnings can be retrieved from this observation. First, the operating mode of the DHR circuit (forced or free flow) does not play a direct role on the thermal stratification increase. Nevertheless, it has an impact (i) on the rate at which the stratification increases; (ii) on the extraction of thermal energy, at the global scale. The difference between the cases is explained by the effect of the operating parameters (forced or natural circulation; AC activated or deactivated) on $\dot{Q}_{DHX}$. Second, once the enhanced stratification is established, it persists in time, as indicated by the low RMS values (shaded area on Fig. 9).

3.2. *Stratification and instability*

As seen on the experimental results, the apparition or not of flow reversals results from the competition between the cooling of the primary circuit by the DHX, and the buoyancy source term from at the IHX. From the analysis of the temperatures pinching at the IHX, it can be concluded that the reversals are linked to the loss of the driving term between the core and the IHX. As seen from Fig. 1, the fluid exiting the plenum and entering the IHX is taken near the bottom of the hot pool. The fluid taken here is strongly subjected to the cooling of the plenum, because of the DHX. As $\dot{Q}_{DHX}$ is approximately ten times $\dot{Q}_{IHX}$, the fluid in the plenum is cooled much quicker than the fluid cooled through the IHX. Thus, the fluid entering the hot leg of the primary circuit is already cold, which in turns annihilates both the heat transfer at the IHX, and the global driving term in the primary circuit.

In turn, the global circulation does not occur anymore, and a secondary flow between the top and bottom of the plenum occurs within the hot pool. By continuity and 3D effects, flow reversals are induced, which

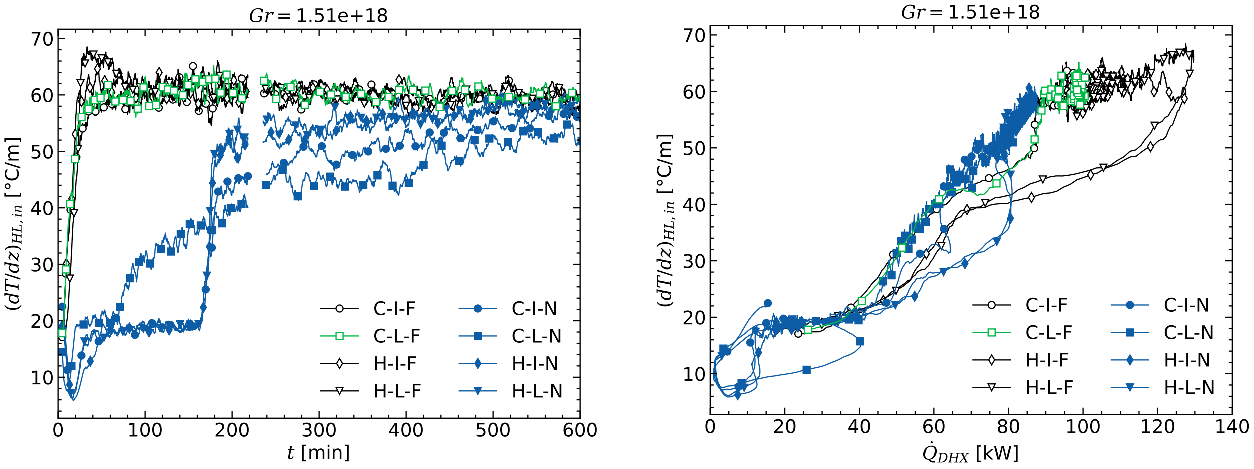

(a)

(b)

Figure 10: Evolution of the stratification with (a) time; (b) $\dot{Q}_{DHX}$.

ultimately leads to removing the cold plug in the primary circuit hot leg. In turn, overall circulation starts again, through the primary circuit.

We use the vertical temperature gradient value near the HL inlet as marker of the thermal stratification, $(dT/dz)_{HL,in} = (dT/dz)_{z=58\text{ mm}}$. The evolution of $(dT/dz)_{HL,in}$ is shown in Fig. 10. We stress that the data shown in Fig. 10 are averaged over a temporal window of 10 min, in order to remove the fast fluctuations of $(dT/dz)_{HL,in}$, and to improve the readability. First, Fig. 10a shows the evolution of $(dT/dz)_{HL,in}$ as a function of time. It is quite striking that $(dT/dz)_{HL,in}$ follows the same evolution as $\dot{Q}_{DHX}$. Indeed, as shown in Fig. 10b, the curves representing the evolution of $(dT/dz)_{HL,in}$ with $\dot{Q}_{DHX}$ all collapse onto a single curve, with a quasi-linear dependence. This shows that the extracted power $\dot{Q}_{DHX}$ directly enhances the stratification, regardless of the heat transfer at the IHX and flow dynamics. It can also be noticed that the response curve is quasi-flat for low $\dot{Q}_{DHX}$. Indeed, for $\dot{Q}_{DHX} \leq 40$ kW, we have a constant stratification level, $(dT/dz)_{HL,in} \approx 20$°C/m. This shows that for low extraction power, there is no increase in stratification, and the establishment of natural circulation should not be perturbed if the power extraction is limited. The same comment can be made for high $\dot{Q}_{DHX} \leq 90$ kW, where the curve is once again flat, showing that a maximum stratification is reached, with $(dT/dz)_{HL,in} \approx 60$°C/m.

In addition, a slight deviation to the master curves is observed for $X_1 = H$ cases. These deviations occur simultaneously with the steep jump in $\dot{Q}_{DHX}$, observed at $t = 10$ min 20 s for $X_3 = F$ cases, and at $t = 160$ min for the $X_3 = N$ cases. This is due to a delay in the stratification response time regarding the $\dot{Q}_{DHX}$ increase. The curves merge back to the master curve after the steep jump. Moreover, in the studied cases, $\dot{Q}_{DHX}$ only increases with the course of the transient. It would be interesting to see if the high stratification persists or evolves if $\dot{Q}_{DHX}$ starts to decrease. Particular attention is dedicated to analyzing the response time of the loop in Section 3.3.

The competition between the heat removal via the DHX and via primary circuit circulation can be analyzed thanks to the Stanton number St. In the case of PLANDTL-2, it is defined as:

$$\mathrm{St} = \frac{\mathrm{Nu}_{DHX}}{\mathrm{Re}_I \, \mathrm{Pr}}. \tag{6}$$

We define the Reynolds number of the primary circuit as:

$$\mathrm{Re}_I = \frac{U_I D_I}{\nu} = \frac{4W_I}{\pi D_I \mu}, \tag{7}$$

the Prandtl number $\mathrm{Pr} = \nu/\kappa$, and the Nusselt number at the DHX as:

$$\mathrm{Nu}_{DHX} = \frac{h_{DHX} H_{DHX}}{\lambda}. \tag{8}$$

We introduce here some thermophysical properties of liquid sodium taken from [30]:

- ν and μ: kinematic and dynamic viscosity;
- ρ: density;
- κ: thermal diffusion coefficient;
- β: thermal expansion coefficient.

Rigorously, St should be defined using steady-state quantities. It is here assumed that the flow and heat transfer evolve slowly and that instantaneous values of the flowrate and heat flux can be used to define St. The time-evolution of St is shown in Fig. 11. We also define the Grashof number, which compares the buoyancy effects to the viscous dissipation, as:

$$\mathrm{Gr} = \frac{D_I^2 \rho^2 \beta g \Delta T}{\mu^2}, \tag{9}$$

$$\Delta T = \frac{\dot{Q}_{elec} H_{core}}{A_c \mu c_p}, \tag{10}$$

with the cross-section $A_c = \pi D_{core}^2/4$. In the studied case, as $\dot{Q}_{elec}$ is constant, the Grashof number is also constant, with $\mathrm{Gr} = 1.51 \times 10^{18}$.

For $X_3 = N$ cases, St always follows the same evolution. It slowly increases towards an asymptotic value $10 \leq \mathrm{St} \leq 20$. For the $X_3 = F$ cases, the evolution differs. First, a steep increase of St is observed in the early moments of the transient. It then stabilizes temporarily, before the onset of instability and reversals around $t \approx 50$ min. It is noticeable that the case *C-L-F* has the lowest St value among the forced case, with $\mathrm{St} \approx 20$.

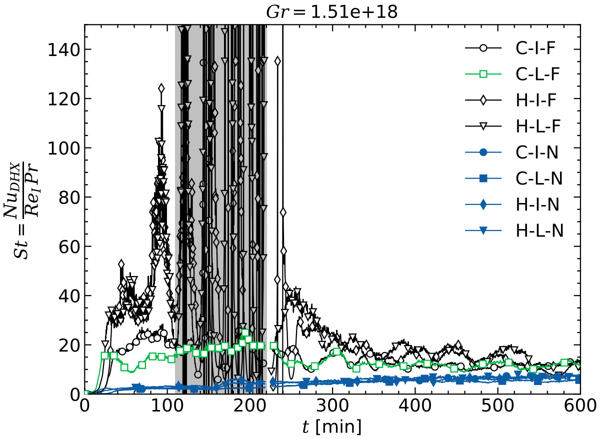

Figure 11: Stanton number of the primary loop over time.

For all cases displaying instability, St > 20. The value St ≈ 20 is therefore the stability threshold for the natural circulation experiments in PLANDTL-2. As St increases, instability and reversal appear in the time slot 110 min $\leq t \leq$ 220 min. During this period of time, St values have no meaning, as the flow cannot be considered as quasi-steady. After the oscillations phase, St slowly decreases and converges towards values St ≤ 20. This threshold value corresponds to the maximal heat that can be stored and conveyed through the primary circuit. We stress here that the value of St ≈ 20 is anecdotal, as it raises from arbitrary choices of length scales in particular. Nevertheless, the stability of the system considered here is subjected to a threshold and the Stanton number as defined here compares the DHX cooling to the circulation through the HL. The results obtained here contradict the presupposed effect of the DHX, which was to cool the plenum while avoiding stratification.

It is clear from these trials that the stratification increase persists in time. Nevertheless, if the circulation through the primary circuit is primed before the increase in stratification, the loop remains stable. Here, high Nu_{DHX} are synonym of high stratification level, whereas high Re_I are synonym of well-primed circulation. The Stanton number St as defined in Eq. (6) compares the stratification in the hot pool to the circulation through the primary circuit. As shown in the present study, it can be used to highlight the stability of the loop.

In addition to these observations, we emphasize that the flow oscillations and stratification do not affect the temperature levels in the core. Indeed, the temperature at the exit of the heated channels, near the of the core, are shown in Fig. 12. First, the flowrate oscillations are not reflected on the temperature evolution, showing that they do not influence the maximal core temperature. This is likely an effect of the IWF, which smooths the temperature evolution. Second, the temperature evolution mainly depends on the operating of the DHR system, i.e. forced or natural circulation. In forced cases, the temperature quickly stabilizes around

390°C in about 30 min. In natural circulation cases, the temperature slowly rises from 400°C to 500°C, as $\dot{Q}_{DHX}$ does not compensate fully the thermal input $\dot{Q}_{elec} = 110$ kW, as shown in Fig. 7. For these cases, the slope decreases as the DHR system AC is activated, at $t = 160$ min. For the case *C-L-N*, the slope is smaller, as the AC is activated at $t = 10$ min 20 s. In all natural circulation cases, the final temperature stabilizes around 500°C.

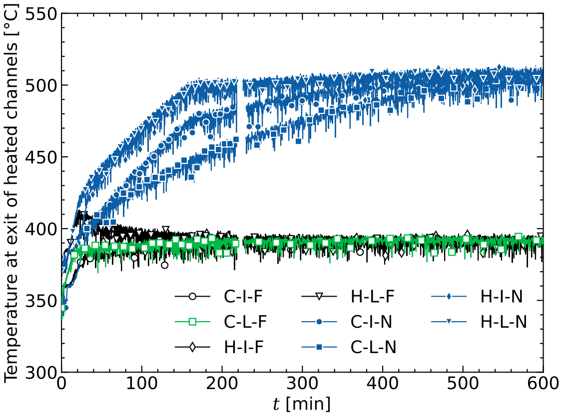

Figure 12: Time-evolution of temperature at the exit of heated channels.

3.3. System response time to the jump in $\dot{Q}_{DHX}$

As seen from Figs. 7 and 10a, the stratification levels follow a similar evolution as $\dot{Q}_{DHX}$, with some delay in time. It is interesting to quantify this delay, as it indicates the response time of the stratification to the modification of the extracted power at the DHX. In particular, a jump $\Delta\dot{Q}_{DHX}$ occurs when the DHR circuit AC is turned on. As stratification plays a key role in the loop stability, it is interesting to quantify more precisely the delay between the jump in extracted power and the stratification increase.

To estimate the response time of the stratification to the abrupt increase in $\dot{Q}_{DHX}$, a time-window around the jump is selected for each case. The re-scaled signals of $\dot{Q}_{DHX}$ and stratification can be written as:

$$A = \frac{\dot{Q}_{DHX} - \mu_{DHX}}{\sigma_{DHX}} \tag{11}$$

$$B = \frac{(dT/dz)_{HL,in} - \mu_{strat}}{\sigma_{strat}} \tag{12}$$

where μ and σ are the average and standard deviation operators over the selected time-window. These transformations are applied in order to have $\mu_A = \mu_B = 0$ and $\sigma_A = \sigma_B = 1$.

Classically, the method used to estimate a time delay, denoted $\tau^\star$, between two signals for which only one observation (of the pair) is available, consists firstly in calculating the deterministic cross-correlation between one signal and the other signal shifted by τ [31]. Then, the optimal time shift $\tau^\star$, for which the similarity between the two signals is greatest, is determined by maximizing the absolute value of the correlation function. This indicates the delay such that the signals are best aligned. For simplicity and without loss of generality, we assume in the following that the signal B is shifted by a positive τ, which consists in practice in assuming the knowledge of a causal relationship between the signals A and B. The notations can easily be extended to the case of a negative τ (e.g. by swapping A and B in the notations), or to any τ, but this would complicate the notations without any real interest here. Considering two discrete time series A and B, the cross-correlation for a discrete shift k is given in its deterministic formulation by:

$$C_{AB}(k) = \sum_n A_n B_{n+k}, \tag{13}$$

where n and $n + k$ are the indices of the discrete time series. Note that, in practice, for two finite non-periodic sequences, the sum is truncated at $N_{max} - k$ terms, where N_{max} is the maximum time index of signal observation. So, to ensure a fair comparison of $C_{AB}(k)$ values calculated for different k, it is preferable to consider the following normalization:

$$\mathfrak{C}_{AB}(k) = \frac{1}{N_{max} - k} C_{AB}(k). \tag{14}$$

The estimate of the "discrete" delay $k^\star$ is given by the arg max of $|\mathfrak{C}_{AB}(k)|$:

$$k^\star = \arg\max_k |\mathfrak{C}_{AB}(k)| \,.$$

The time delay $\tau^\star$ is then deduced by $\tau^\star = k^\star \delta t$, where $\delta t = 1/f_s$ and f_s is the signal sampling rate. Note that Eq. (13) is the deterministic formulation of cross-correlation, as opposed to the stochastic cross-correlation of a pair of random processes. The latter is calculated for two given times and is defined as the statistical correlation (i.e. Pearson correlation) between the values of the two processes for these two instants (see [32]). We can then compute the time average of this stochastic cross-correlation using double time integration. Stochastic cross-correlation takes into account signal variability and is more robust to noise than deterministic correlation, but it requires several realizations of the signal, which is not possible in our case. Consequently, only the deterministic formulation can be considered here.

However, the analogy between deterministic and stochastic correlation paves the way for a deterministic extension of other, more powerful, stochastic dependence measures than the simple Pearson correlation. Indeed, Pearson correlation, by definition, only takes into account a linear form of dependency between signals, unlike other broader-spectrum statistical measures which can detect highly non-linear dependencies. Among these, the distance correlation [33] is of particular interest: on the one hand, its nullity is equivalent to probabilistic independence, and on the other hand, its statistical estimation is highly accurate even for limited sample sizes, making it a dependency measure of first choice in many applications [34]. For signal processing applications, the concept of distance correlation has been extended by [35] to propose an auto-distance (or cross-distance for 2 signals) correlation function to measure the temporal dependence structure (linear but also non-linear) in time series. But again, this cross-distance is a stochastic formulation that requires multiple signal realizations.

Based on these considerations and relying on the analogy between deterministic correlation and statistical correlation, we propose to consider a "deterministic" version of the cross-distance correlation as a relevant alternative to deterministic cross-correlation. For this, we first define the cross-distance covariance for two discretized signals A and B as:

$$D_{AB}(k) = \sqrt{\sum_{n} \sum_{l} \tilde{a}_{n,l} \, \tilde{b}_{n+k,l+k}}, \tag{15}$$

where $\tilde{a}_{n,l}$ (resp. $\tilde{b}_{n,l+k}$) are all doubly centered pairwise distances computed for signal A (resp. for signal B shifted by k). More precisely $\tilde{a}_{n,l}$ is defined by:

$$\tilde{a}_{n,l} := a_{n,l} - \overline{a}_{n\bullet} - \overline{a}_{\bullet l} + \overline{a}_{\bullet\bullet}, \tag{16}$$

where

$$\begin{aligned} a_{n,l} &= |A_n - A_l|, & \overline{a}_{n\bullet} &= \sum_{l} a_{n,l}, \\ \overline{a}_{\bullet l} &= \sum_{n} a_{n,l}, & \overline{a}_{\bullet\bullet} &= \sum_{l} \sum_{n} a_{n,l}. \end{aligned} \tag{17}$$

Similar notations apply to $\tilde{b}_{n+k,l+k}$ values. Moreover, for discrete finite series, each sum is truncated at $N_{max} - k$ terms. So, as for C_{AB}, it is more accurate to consider the following normalization:

$$\mathcal{D}_{AB}(k) = \frac{1}{N_{max} - k} D_{AB}(k). \tag{18}$$

Finally, we can define a cross-distance correlation by dividing $\mathcal{D}_{AB}(k)$ by the square root of the product of the distance covariances of each signal (as it is done to define the distance correlation from distance covariance):

$$\mathfrak{D}_{AB}(k) = \frac{\mathcal{D}_{AB}(k)}{\sqrt{\mathcal{D}_{AA}(0)\mathcal{D}_{B_k B_k}(0)}}. \tag{19}$$

where B_k denotes the signal B shifted by k. Finally, $k^\star$ is estimated by $k^\star = \arg\max_k \mathfrak{D}_{AB}(k)$ and $\tau^\star$ is deduced, as for $\mathfrak{C}_{AB}$. To illustrate the performance of $\mathfrak{D}_{AB}$ and compare it with that of $\mathfrak{C}_{AB}$ for estimating $\tau^\star$, we carried out a benchmark on virtual signals generated with a known $\tau^\star$, and that closely mimics the signals observed in our application (similar shape and noise level). More precisely, the generated signals have a prescribed delay $\tau^\star \in [1, 7]$ min and a noise level $\sigma_B \in [0.1, 0.6]$. These ranges were chosen because they encompass the empirical observations. This benchmark on virtual data and the results obtained are presented in Appendix A: they show that $\mathfrak{D}_{AB}$ yield more reliable estimates of $\tau^\star$ than $\mathfrak{C}_{AB}$, for the type of signals considered.

Strengthened by these results, $\mathfrak{D}_{AB}$ is then applied to the observed signals. The plot of $\mathfrak{D}_{AB}$ according to τ is given by Fig. 13a and shows that the estimated delay is 3 min 19 s for the case *H*-*L*-*N*. Fig. 13b shows the re-scaled *A* and *B* signals, and the re-timed *B* signal (delayed by 3 min 19 s): a good agreement is observed between the *A* signal and the re-timed *B* signal.

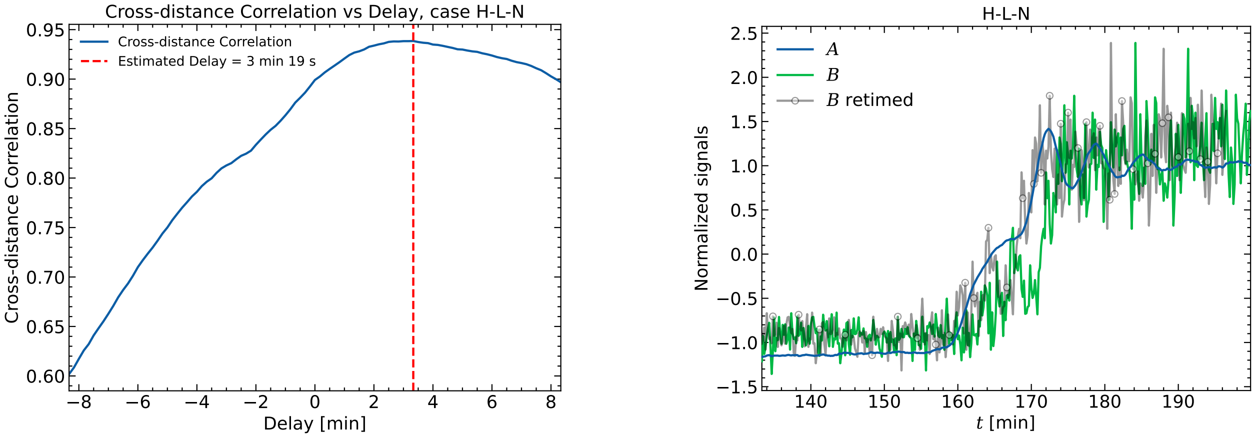

(a) Delay estimated with the cross-distance correlation method.

(b) Re-scaled *A* and *B* signals; and re-timed *B* signal.

Figure 13: Delay estimate for *H*-*L*-*N* case.

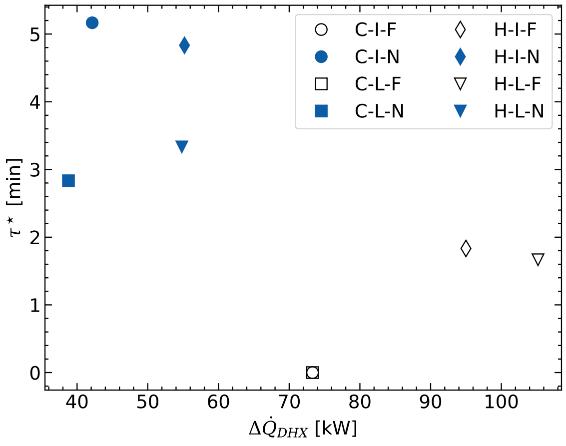

Figure 14: Evolution of the response time $\tau^\star$ with the jump $\Delta\dot{Q}_{DHX}$.

The delay estimate process based on cross-distance correlation is repeated for all cases. As shown in Fig. 14, it is striking that the response time depends on $\Delta\dot{Q}_{DHX}$. For lower $\Delta\dot{Q}_{DHX}$ (i.e. $X_3 = N$ cases), the response time is $\tau \approx 5$ min, whereas for higher $\Delta\dot{Q}_{DHX}$ (i.e. $X_3 = F$ cases), the response time is $\tau \approx 1$ min.

The typical Reynolds number $\mathrm{Re}_{pl} = U_{pl}H_{pl}/\nu$ for the buoyant plumes in the hot pool can be estimated thanks to typical scaling laws for Rayleigh-Bénard convection [36] as a function the effective Rayleigh number Ra_{pl} inside the plenum:

$$\mathrm{Re}_{pl} \sim \mathrm{Ra}_{pl}^{1/2}\mathrm{Pr}^{-3/4} \tag{20}$$

$$\text{with } \mathrm{Ra}_{pl} = \frac{g\beta\Delta T_{pl}H_{pl}^3}{\nu\kappa}, \tag{21}$$

and H_{pl} the plenum height, ΔT_{pl} a characteristic temperature difference for buoyancy. Here it is taken between the bottom and top of the UIS, at the center of the pool, and it is weakly on the transient scenario. Finally, assuming a unit proportionality constant, this leads to the typical timescale of the buoyant plumes:

$$\tau_{buoy} = \frac{H_{pl}}{U_{pl}} = \frac{H_{pl}^2}{\nu}\mathrm{Ra}_{pl}^{-1/2}\mathrm{Pr}^{3/4} = 1\,\mathrm{min}\ 16\,\mathrm{s} \pm 15\,\mathrm{s}. \tag{22}$$

As $\tau^\star$ and τ_{buoy} have the same order of magnitude, the stratification process and buoyant motions in the plenum interact strongly. In cases where the response time $\tau^\star$ is quick compared to the buoyant plumes timescale τ_{buoy}, stratification increase becomes the dominant mechanism. In such cases, there is a risk to impede the proper establishment of natural circulation throughout the primary circuit. These findings are consistent with the instability mechanism proposed in Section 3.2.

4. Conclusions

Sodium natural circulation tests were carried out on the PLANDTL-2 experiment. The purpose was to understand the effect of several parameters on the global flow dynamics in this IET, and also to develop a database for multiscale codes validation. Long term instabilities and reversals were observed in the time frame $t = 110$ min to 220 min, but only for cases where the heat removal by the DHX is strongly dominant. This means that instability is observed when the primary circuit is quickly cooled. This counter-intuitive observation is actually due to the combination strong plenum cooling by the DHX and high stratification level near the entrance of the HLs. This increase in thermal stratification is enhanced by the DHR circuit forced circulation, combined with its AC system. These effects are unfavorable to natural circulation at the circuit scale. They are tempered by the heat evacuation via convection through the primary circuit. The comparison of these contributions can be analyzed using the Stanton number, which compares the cooling due to the DHX to the convection in the primary circuit. It is found that stable circulation occurs below a threshold Stanton number, which value depends on the loop geometry.

In addition, a method to estimate the system response time was developed. The results highlighted that the stratification response time was dependent on the jump in DHX extracted power, when the AC is turned on. The stratification increase is quicker as the jump in $\dot{Q}_{DHX}$ is higher. In order to maintain the flowrate stability, it is needed that the rise in $\dot{Q}_{DHX}$ remains low, so that it does not interfere with the establishment of natural circulation.

As PLANDTL-2 is designed to be representative of actual pool type SFR concepts, such as ASTRID, some guidelines to avoid flow instability can be given:

1. the cooling rate of the DHX needs to be limited to avoid pinching at the IHX;
2. or conversely, the DHX activation needs to be delayed after the full priming of circulation in the primary circuit;
3. hot fluid circulation towards the primary circuit HL can be privileged by having the hot leg piping higher in the plenum (avoid the stratification issue) or by increasing the elevation of the DHX;
4. completely close the primary circulation and remove global circulation. The core cooling is thus ensured by the DHX only and the prefered flow path goes through the IWG;
5. increase mixing in the plenum to avoid stratification by using passive vannes for example.

These guidelines are not necessarily compatible among each others and experimental investigation remains necessary in order to evaluate which ones are of interest for the design of passive safety devices for SFRs. Moreover, the expected benefits of the proposed guidelines should be balanced by the effect on the maximum core (and more precisely cladding) temperature. As a matter of fact, in PLANDTL-2, the flowrate oscillations do not impact the core temperature evolution, but this conclusion can be hard to be generalized to all concepts and accidental transients. The operating mode of the DHR system (i.e. $\dot{Q}_{DHX}$) remains the main parameter affecting the core temperature in this case.

In the framework of code validation, this work shows that 3D effects such as stratification play a key role in the global dynamics. Consequently, 0D homogeneous models cannot be used to properly represent the dynamics in the plenum. Thus, the use of 3D codes, such as CFD codes or multiscale coupled strategies are necessary to capture even the long term dynamics ($t \geq 100$ min) of these systems. Another possible approach is the 1D modeling of the pool stratification in the vertical direction.

Acknowledgments

Authors acknowledge fruitful discussions with Antoine Gerschenfeld and Yannick Gorsse. This work is the result of the collaboration agreement between CEA and JAEA. The transient scenarios were defined jointly and the experiments carried out by JAEA. Analysis and interpretation of the tests were done in CEA based on data provided by JAEA. The authors are grateful to their respective organizations for enabling this collaborative work.

Appendix A. Benchmark of Methods for Optimal Time Shift Estimation

The aim here is to compare the two methods cited in Section 3.3 for estimating the optimal delay $\tau^\star$. More precisely, we want to evaluate the performance of the method based on cross-distance correlation $\mathfrak{D}_{AB}$ (Eq. (19)), compared to the standard cross-correlation method $\mathfrak{C}_{AB}$ (Eq. (14)). To do this, we run a benchmark on virtual signals that are representative of the signals of the application case, but for which we know the theoretical delay. More precisely, we consider for signal A the re-scaled signal $\dot{Q}_{DHX}$ (Eq. (11)) of test-case H-L-N. And for signal B, we simulate a virtual signal as equal to signal A shifted by $\tau^\star$ plus a white noise of constant standard deviation σ_B. The objective is then to recover the prescribed delay $\tau^\star$ from the single observation of the pair of signals (A,B), applying either the cross-correlation $\mathfrak{C}_{AB}$ or the cross-distance correlation $\mathfrak{D}_{AB}$. The optimal time delays estimated with both methods are respectively denoted $\hat{\tau}^\star_{\mathfrak{C}}$ and $\hat{\tau}^\star_{\mathfrak{D}}$ and are then compared to the prescribed delay $\tau^\star$. In practice, this procedure is carried out for different delay $\tau^\star$ values ranging from 2 min to 6 min 30 s, and for σ_B values ranging from 0.1 to 0.7. Moreover, for each combination of $\tau^\star$ and σ_B, 50 repetitions are performed with independent and identically distributed noise realizations. Each time, the relative absolute error $\mathrm{RAE}_{\hat{\tau}^\star} = \left|\frac{\hat{\tau}^\star - \tau^\star}{\tau^\star}\right|$ is computed for each of the 2 methods. The mean value $\mathrm{MRAE}_{\hat{\tau}^\star}$, over the 50 repetitions, is given by Figure A.15, as a function of $\tau^\star$ and σ_B.

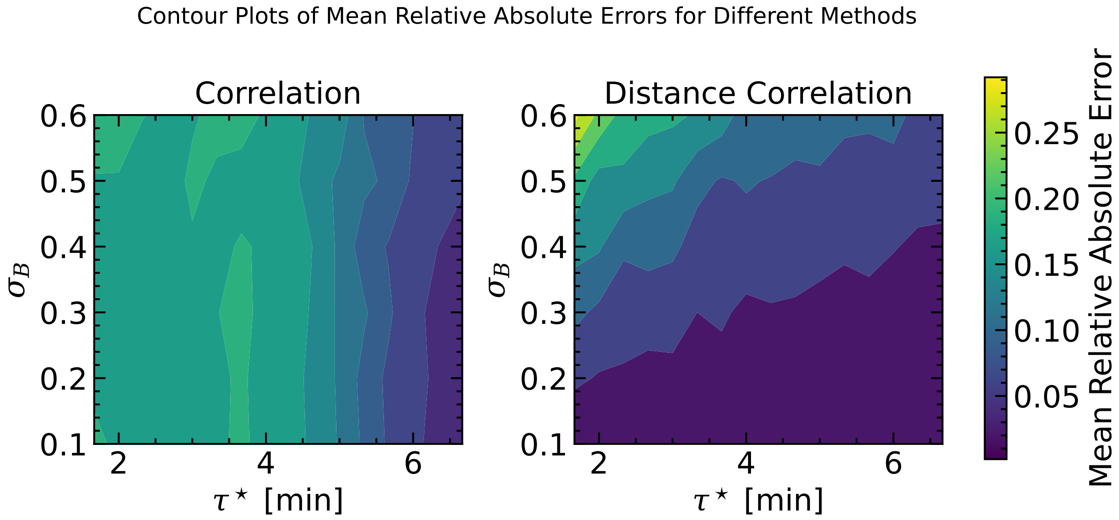

Figure A.15: Mean Relative Absolute Error according to prescribed delay $\tau^\star$ and standard deviation of noise σ_B. The cross-correlation $\mathfrak{C}_{AB}$ and cross-distance correlation $\mathfrak{D}_{AB}$ are defined in Eqs. (14) and (19), respectively.

The results show that the cross-distance correlation leads to a more accurate estimate of the delay over the whole range of $\hat{\tau}^\star$ and σ_B considered. Cross-distance correlation produces an $\mathrm{MRAE}_{\hat{\tau}^\star}$ four times smaller for noise levels lower than 0.4. This superiority then tends to decrease for higher noise levels. In addition, we can analyze the estimates for specific $\tau^\star$ and σ_B values. Let us consider, for example, the case

$\tau^\star = 4$ min 20 s and $\sigma_B = 0.3$, which are close to those of the observed signals, as illustrated by a basic denoising of signal B using a low-pass Butterworth filter (Figure A.16). We find a mean absolute error of around 40 s (mean relative error of $\sim$ 20%) with a standard deviation of 5 s for the standard cross-correlation $\mathfrak{C}_{AB}$, compared with a mean error equal to 10 s (mean relative absolute error of $\sim$ 5%) with a standard deviation of 10 s for the correlation cross-distance $\mathfrak{D}_{AB}$. This virtual specific example, close to the real case, gives us an insight into the estimation error of each method.

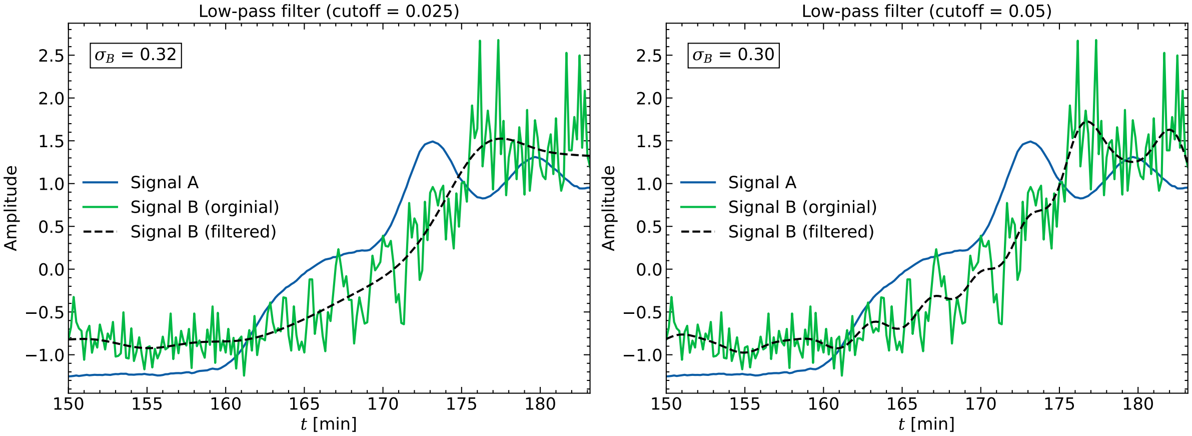

Figure A.16: Illustration of signal B denoising using a low-pass filter with different filter parameters on the *H*-*L*-*N* case. The estimated standard deviation of noise σ_B is indicated in each case.

References

[1] F. Varaine, G. Rodriguez, J. Hamy, S. Kubo, H. Mochida, U. Yukinori, J. Helle, A. Remy, T. Chauveau, J. Mazel, et al., ASTRID project, general overview and status progress, in: GIF Symposium-the 4th GIF Symposium at the 8th edition of Atoms for the Future, 2018.

[2] S. Li, S. Bajard, B. Grosjean, L. Matteo, A. Gerschenfeld, Y. Gorsse, M. Anderhuber, Multi-scale thermal hydraulics calculations of FFTF ”loss of flow without scram” transient with MATHYS, in: 19th international topical meeting on Nuclear Reactor Thermal Hydraulics (NURETH 19), 2022.

[3] U. Parthasarathy, T. Sundararajan, C. Balaji, K. Velusamy, P. Chellapandi, S. Chetal, Decay heat removal in pool type fast reactor using passive systems, Nuclear Engineering and Design 250 (2012) 480–499.

[4] G. Vaidyanathan, Decay heat removal in sodium cooled fast reactors-an overview, Annals of Nuclear Energy 205 (2024) 110554.

[5] F. Roelofs, Thermal hydraulics aspects of liquid metal cooled nuclear reactors, Woodhead Publishing, 2018.

[6] N. Kimura, H. Miyakoshi, H. Kamide, Experimental study on thermal stratification in a reactor vessel of innovative sodium-cooled fast reactor—mitigation approach of temperature gradient across stratification interface—, Journal of nuclear science and technology 47 (9) (2010) 829–838.

[7] M. Tarantino, D. Martelli, G. Barone, I. Di Piazza, N. Forgione, Mixed convection and stratification phenomena in a heavy liquid metal pool, Nuclear Engineering and Design 286 (2015) 261–277.

[8] M. Y. Ali, G. Wu, S. Liu, M. Jin, Z. Zhao, Y. Wu, CFD analysis of thermal stratification under PLOFA transient in CLEAR-S, Progress in Nuclear Energy 115 (2019) 21–29.

[9] D. Grishchenko, A. Papukchiev, C. Liu, C. Geffray, M. Polidori, K. Kööp, M. Jeltsov, P. Kudinov, Tall-3d open and blind benchmark on natural circulation instability, Nuclear Engineering and Design 358 (2020) 110386.

[10] D. Pialla, D. Tenchine, S. Li, P. Gauthe, A. Vasile, R. Baviere, N. Tauveron, F. Perdu, L. Maas, F. Cocheme, et al., Overview of the system alone and system/CFD coupled calculations of the PHENIX Natural Circulation Test within the THINS project, Nuclear Engineering and Design 290 (2015) 78–86.

[11] Z. Wu, C. Lu, S. Morgan, S. B. y Leon, M. Bucknor, A status review on the thermal stratification modeling methods for sodium-cooled fast reactors, Progress in Nuclear Energy 125 (2020) 103369.

[12] Y. Liu, D. Zhang, L. Zhou, K. Chen, W. Tian, S. Qiu, G. Su, Analysis of the effect of thermal stratification on the natural circulation decay heat removal of sodium-cooled fast reactor, Progress in Nuclear Energy 167 (2024) 104979.

[13] M. Azarian, M. Astegiano, M. Tenchine, M. Lacroix, M. Vidard, Sodium thermal-hydraulics in the pool lmfbr primary vessel, Nuclear Engineering and Design 124 (3) (1990) 417–430.

[14] J. Yoon, J. Lee, H. Kim, Y.-B. Lee, J. Eoh, Heat transfer characteristics of redan structure in large-scale test facility STELLA-2, Nuclear Engineering and Technology 53 (4) (2021) 1109–1118.

[15] J. Lee, J. Eoh, J. Yoon, S.-K. Son, H. Kim, Heat transfer system design of sodium test facility STELLA-2, Annals of Nuclear Energy 191 (2023) 109930.

[16] H. Zhao, P. F. Peterson, An overview of modeling methods for thermal mixing and stratification in large enclosures for reactor safety analysis, in: 8th International Topical Meeting on Nuclear Thermal-Hydraulics, Operation and Safety (NUTHOS-8), Shanghai, China, 2010.

[17] M. Nishimura, H. Kamide, K. Hayashi, K. Momoi, Transient experiments on fast reactor core thermal-hydraulics and its numerical analysis: Inter-subassembly heat transfer and inter-wrapper flow under natural circulation conditions, Nuclear Engineering and Design 200 (1-2) (2000) 157–175.

[18] T. Ezure, Y. Akimoto, T. Onojima, M. Kurihara, A. Tanaka, Transient behavior of multi-dimensional core cooling by d-dhx in sodium-cooled fast reactors, in: Proceedings of the 20th International Topical Meeting on Nuclear Reactor Thermal Hydraulics (NURETH-20), Washington, USA, 2023.

[19] J. Boure, A. Bergles, L. S. Tong, Review of two-phase flow instability, Nuclear Engineering and Design 25 (2) (1973) 165–192.

[20] L. C. Ruspini, C. P. Marcel, A. Clausse, Two-phase flow instabilities: A review, International Journal of Heat and Mass Transfer 71 (2014) 521–548.

[21] Q. Wang, P. Gao, X. Chen, Z. Wang, Y. Huang, An investigation on flashing-induced natural circulation instabilities based on RELAP5 code, Annals of Nuclear Energy 121 (2018) 210–222.

[22] S. Renaudière de Vaux, P. Aubert, B. Grosjean, L. Rossi, Flow reversals in a natural circulation loop at atmospheric pressure, International Journal of Heat and Mass Transfer 235 (2024) 126119. `doi:https://doi.org/10.1016/j.ijheatmasstransfer.2024.126119`.

[23] P. Vijayan, H. Austregesilo, V. Teschendorff, Simulation of the unstable oscillatory behavior of single-phase natural circulation with repetitive flow reversals in a rectangular loop using the computer code athlet, Nuclear Engineering and Design 155 (3) (1995) 623–641.

[24] P. Vijayan, Experimental observations on the general trends of the steady state and stability behaviour of single-phase natural circulation loops, Nuclear Engineering and Design 215 (1-2) (2002) 139–152.

[25] M. Misale, Experimental study on the influence of power steps on the thermohydraulic behavior of a natural circulation loop, International Journal of Heat and Mass Transfer 99 (2016) 782–791.

[26] P. K. Vijayan, A. K. Nayak, N. Kumar, Single-phase, two-phase and supercritical natural circulation systems, Woodhead Publishing, 2019.

[27] A. Ono, M. Tanaka, Y. Miyake, E. Hamase, T. Ezure, Preliminary analysis of sodium experimental apparatus plandtl-2 for development of evaluation method for thermal-hydraulics in reactor vessel of sodium fast reactor under decay heat removal system operation condition, Mechanical Engineering Journal 7 (3) (2020) 19–00546.

[28] H. Kamide, T. Asayama, T. Wakai, T. Ezure, A. Uchibori, S. Kubo, M. Takeuchi, Progress of sodium-cooled fast reactor developments in japan taking into account total lifecycle, risk-informed approach, and sustainability, Nuclear Engineering and Design 421 (2024) 113062.

[29] P. Vijayan, M. Sharma, D. Saha, Steady state and stability characteristics of single-phase natural circulation in a rectangular loop with different heater and cooler orientations, Experimental Thermal and Fluid Science 31 (8) (2007) 925–945.

[30] G. Rodriguez, Le caloporteur sodium (mise à jour de l'article de 2004), Techniques de l'Ingénieur (2018).

[31] R. Bracewell, Pentagram notation for cross correlation, in: The Fourier Transform and Its Applications, McGraw-Hill, New York, 1965, p. 46 and 243.

[32] G. Box, G. M. Jenkins, Time Series Analysis: Forecasting and Control, Holden-Day, 1976.

[33] G. J. Székely, M. L. Rizzo, N. K. Bakirov, Measuring and testing dependence by correlation of distances, The Annals of Statistics 35 (6) (2007) 2769–2794.

[34] M. De Lozzo, A. Marrel, New improvements in the use of dependence measures for sensitivity analysis and screening, Journal of Statistical Computation and Simulation 86 (15) (2016) 3038–3058.

[35] Z. Zhou, Measuring nonlinear dependence in time-series, a distance correlation approach, Journal of Time Series Analysis 33 (3) (2012) 438–457.

[36] S. Grossmann, D. Lohse, Scaling in thermal convection: a unifying theory, Journal of Fluid Mechanics 407 (2000) 27–56.